



**HAL**  
open science

## Statistics of velocity fluctuations in a homogeneous liquid fluidized bed

Élise Alméras, Frederic Risso, Olivier Masbernat, Rodney O. Fox

► **To cite this version:**

Élise Alméras, Frederic Risso, Olivier Masbernat, Rodney O. Fox. Statistics of velocity fluctuations in a homogeneous liquid fluidized bed. *Physical Review Fluids*, 2021, 6 (3), pp.034301. 10.1103/PhysRevFluids.6.034301 . hal-03181075

**HAL Id: hal-03181075**

**<https://hal.science/hal-03181075v1>**

Submitted on 25 Mar 2021

**HAL** is a multi-disciplinary open access archive for the deposit and dissemination of scientific research documents, whether they are published or not. The documents may come from teaching and research institutions in France or abroad, or from public or private research centers.

L'archive ouverte pluridisciplinaire **HAL**, est destinée au dépôt et à la diffusion de documents scientifiques de niveau recherche, publiés ou non, émanant des établissements d'enseignement et de recherche français ou étrangers, des laboratoires publics ou privés.



## Open Archive Toulouse Archive Ouverte



OATAO is an open access repository that collects the work of Toulouse researchers and makes it freely available over the web where possible

This is an author's version published in: <https://oatao.univ-toulouse.fr/27533>

### Official URL:

<https://doi.org/10.1103/PhysRevFluids.6.034301>

### To cite this version:

Alméras, Élise  and Risso, Frédéric  and Masbernat, Olivier  and Fox, Rodney O. *Statistics of velocity fluctuations in a homogeneous liquid fluidized bed*. (2021) *Physical Review Fluids*, 6 (3). 034301. ISSN 2469-990X.

Any correspondence concerning this service should be sent to the repository administrator: [tech-oatao@listes-diff.inp-toulouse.fr](mailto:tech-oatao@listes-diff.inp-toulouse.fr)

# Statistics of velocity fluctuations in a homogeneous liquid fluidized bed

Elise Alméras

*FR FERMAT, Université de Toulouse,  
CNRS, INPT, UPS, Toulouse, France*

Frédéric Risso

*Institut de Mécanique des Fluides de Toulouse (IMFT),  
Université de Toulouse, CNRS, Toulouse, France*

Olivier Masbernat

*Laboratoire de Génie Chimique (LGC), CNRS-INPT-UPS,  
Université de Toulouse, 31400 Toulouse, France*

Rodney O. Fox

*Department of Chemical and Biological Engineering,  
618 Bissell Road, Iowa State University, Ames, IA 50011-1098, USA*

(Dated: February 19, 2021)

## Abstract

This work reports an experimental investigation of a liquid-solid fluidized bed involving inertial particles at large Reynolds number. Thanks to optical techniques and index matching, the statistics of the velocity fluctuations of both the particles and the liquid are measured for a wide range of the particle volume fraction  $\alpha_p$ . The dynamics of the fluctuations suggests that the flow possesses the three following properties: (1) The liquid volume involves a wake region in which vertical fluctuations are negative and an interstitial region where they are positive; (2) The statistics of the horizontal fluctuations are similar to vertical ones, except that they are symmetric; (3) Local instant particle fluctuations are proportional to liquid ones. Assuming these properties are true allows us to derive a model for the probability density functions (p.d.f.s) of the two components of the velocity fluctuations of the two phases. This model involves a single reference p.d.f. that is independent of  $\alpha_p$  and one weighting parameter for each phase. The weighting parameter of the liquid phase is an affine function of  $\alpha_p$ , which characterizes the volume of the wakes relative to that of the interstices. That of the particle phase depends on the preferential concentration of the particles, which tend to avoid the wakes at low  $\alpha_p$ . This model accurately describes the experimental p.d.f.s up to the third-order moment and reproduces all their peculiar features: skewness of the vertical fluctuations which reverses at a given volume fraction, presence of exponential tails corresponding to rare intense events, symmetry between low and large volume fractions.

Keywords: Two-phase flow, Fluidized bed, Velocity fluctuations, Probability density function

## I. INTRODUCTION

We report experimental investigations of the velocity statistics in liquid-solid fluidized beds at large Reynolds number, in which dense particles are supported by a continuous upward flow of a liquid. In contrast with gas-solid fluidized beds, the spatial distribution of the particles in such configurations remains statistically uniform over a large range of particle volume fraction  $\alpha_p$ , typically from 0.1 to 0.5. Both phases experience strong velocity fluctuations that result from the drift velocity between them, which is itself due to gravity. Because of this agitation, liquid fluidized beds are an efficient tool for enhancing heterogeneous chemical reactions or interfacial mass transfer, in particular in crystallization or biofilm growth processes (see [1] and references therein). In addition, they build a configuration of dispersed two-phase flow that is especially interesting to study the complex interplay between the fluctuating motions of the two phases in cases where the dispersed phase is homogeneous while its concentration is large.

In dispersed two-phase flows, whatever the nature the dispersed phase (liquid, gaseous or solid particles), the agitation of the continuous phase that is induced by the relative motion of the particles generally involves two contributions [2–4]: (1) the flow disturbances generated in the vicinity of the particles and (2) the turbulence that results from the collective instability of the flow through a random distribution of obstacles. At low to moderate volume fractions ( $\alpha_p \lesssim 0.1$ ), the mechanisms of the particle-induced fluctuations have been extensively studied in bubble columns (see [5] for a recent review) and the turbulence contribution was found to play an important role, provided the bubble Reynolds number is larger than 100. Regarding large volume fractions ( $\alpha_p > 0.1$ ), we found only a few recent studies that have investigated fluidized beds by means of numerical simulations ([6], [7], [8]). In such configurations, the distance between the particles is too small for turbulence to freely develop and fluctuations are thus dominated by the flow disturbances around each particle.

On the other hand, the particle fluctuations can be seen as a reaction to the liquid fluctuations, in a similar way as in the Tchen-Hinze theory that described turbulent particle-laden flows by considering that the particles respond to the various scales of the prescribed turbulent fluctuations in an amount which depends upon their inertia ([9], [10], [11]). However, in contrast to turbulent particle-laden flows, the liquid fluctuations in a fluidized bed are a direct consequence of the presence of the particles. The coupling between the liquid and

particle fluctuations is therefore much stronger and necessarily depends upon the particle volume fraction. Over several decades, numerous works have addressed the problem of the particle agitation in liquid fluidized beds ([12], [13], [14], [15], [16], [17], [18], [19]). Despite this continuous effort and the growing capabilities in numerical simulations, a physical model relating the particle agitation to the particle-induced liquid agitation is still lacking. This is primarily due to a lack of experiments in which measurements of the velocity statistics of the two phases are jointly measured, especially in dense inertial suspensions ([20], [21]).

The present work provides extensive measurements of the statistics of the velocity fluctuations of the liquid and the particles in a liquid-solid fluidized bed involving inertial particles with a particle-to-liquid density ratio of 1.5, a Reynolds number in between 150 and 360, at concentrations ranging from 0.14 and 0.42. In a recent Rapid Communication to Phys. Rev. Fluids [22], a first analysis of these results was presented, limited to the second-order moments of the fluctuations. A physical interpretation of the mechanism controlling the energy of the fluctuations was proposed, leading to a model for the velocity variances of both phases. The main idea was to distinguish two regions within the liquid: (1) the wakes of the particles in which the liquid is entrained at the velocity of the particle; (2) the interstitial region between the particles where the liquid velocity is close to its average value. This suggests assuming that the random fluctuation of each component  $u'_i$  of the liquid velocity is proportional to the product of the average liquid velocity  $\langle U_z \rangle$  and the fluctuation  $\chi'$  of the solid-phase indicator function, which characterizes the fluctuations of the concentration:  $u'_z = -\gamma_z \langle U_z \rangle \chi'$ . A simple model is thus obtained that relates the variance of the liquid velocity to that of the solid-phase indicator function:  $\langle \chi'^2 \rangle = \alpha_p(1 - \alpha_p)$ . The standard deviation of each component liquid velocity then reads

$$\sqrt{\langle u'^2_i \rangle} / \langle U_z \rangle = \gamma_i \sqrt{\alpha_p(1 - \alpha_p)}. \quad (1)$$

This model nicely fits the experimental results in the whole range of solid phase fraction investigated ( $0.14 \leq \alpha_p \leq 0.42$ ) by taking  $\gamma_z = 1.24$  for the vertical direction and  $\gamma_x = 0.79$  for the horizontal one.

Regarding the velocity fluctuations  $v'_i$  of the particles, we assume that the fluctuation of the slip velocity  $u'_i - v'_i$  is controlled by the same mechanism as the one which determines the fluidization law relating the mean liquid velocity  $\langle U_z \rangle$  to the mean particle concentration  $\alpha_p$ . This implies that  $u'_i - v'_i = k_i \frac{d\langle U_z \rangle}{d\alpha_p} \chi'$  and leads to the following relation for the standard

deviations of the components of the particle velocity

$$\frac{\sqrt{\langle v_i'^2 \rangle}}{\sqrt{\langle u_i'^2 \rangle}} = \left( 1 + \frac{k_i}{\sqrt{\langle u_i'^2 \rangle}} \frac{d\langle U_z \rangle}{d\alpha_p} \sqrt{\alpha_p(1 - \alpha_p)} \right). \quad (2)$$

This model well reproduces the experimental results by taking  $k_z = 0.35$  for the vertical component and  $k_x = 0.21$  for the horizontal one.

In the present article, we examine the probability density functions (p.d.f.s) of the velocity fluctuations of the two phases. We show that considering the variance of the solid-phase indicator function is not sufficient to model the evolution with  $\alpha_p$  of the p.d.f.s of the velocity fluctuations. The asymmetry of the fluctuations between the wake region and the interstitial region must also be accounted for. That being done, the p.d.f.s of the two velocity components of the two phases for all volume fractions can be related to a single p.d.f., which confirms our physical interpretation based on the distinction between two regions.

The paper is organized as follows. The experimental setup and the physical properties of the two phases are presented in section II. The techniques used to measure the velocity fields of both phases are detailed in section III. Experimental results are presented in section IV: the flow homogeneity is assessed by examining the pair correlation function of the particles in IV A; statistical moments and p.d.f.s of the liquid fluctuations are presented in VB for the liquid and in IVC for the particles. In section V, a model of the p.d.f.s based on the distinction between the wake and the interstitial regions is proposed. Concluding remarks are given in section VI.

## II. EXPERIMENTAL SETUP AND PHASE PROPERTIES

### A. Experimental setup

The fluidization column is schematized in figure 1. It is composed of a cylindrical glass column of internal diameter  $d=51\pm 1$  mm diameter and height  $H=280$  mm. Upstream of the bed entry is mounted a stack of a 20 mm high metal honeycomb of 4 mm meshsize, a 30 mm-high fixed bed of 3 mm metal beads, a thin layer of a synthetic foam topped with a thin mesh metal grid, the whole placed in a conical tube of 70 mm length and 30° semi-angle. This set-up ensures a good homogeneity of the pressure distribution in the liquid at the bed entry. The outlet section, located above the top of the fluidized bed, is a free surface where

the liquid overflows, which limits unwanted boundary effects. The liquid phase is stored in a 30-L tank from which it is pumped into the circuit by means of a centrifugal pump. The particles are made of fluoropolymer Nafion with a density  $\rho_p = 1595 \text{ kg/m}^3$ . They are slightly ellipsoidal, with an equivalent diameter  $d_p = 4 \text{ mm}$  and an aspect ratio of 0.9. Nafion was chosen because of its low refractive index ( $\approx 1.34$ ), making possible optical index adjustment with an ordinary aqueous mixture. The circulating liquid used in the present study is an aqueous solution of glycerine at 17 %w/w, of density  $\rho_l = 1045 \text{ kg/m}^3$ , viscosity  $\mu = 1.76 \times 10^{-3} \text{ Pas}$  and of same optical index as that of Nafion particles. The whole system is maintained at constant temperature ( $T = 19^\circ\text{C}$ ) thanks to a secondary heat-exchange circuit. A transparent double-jacket square section filled with the water-glycerine mixture is placed around the fluidizing column in order to reduce the optical distortions resulting from the column curvature. All measurements are performed in a region located 55 mm above the bottom of the bed and 5 mm from the wall sides, where the flow homogeneity is achieved.

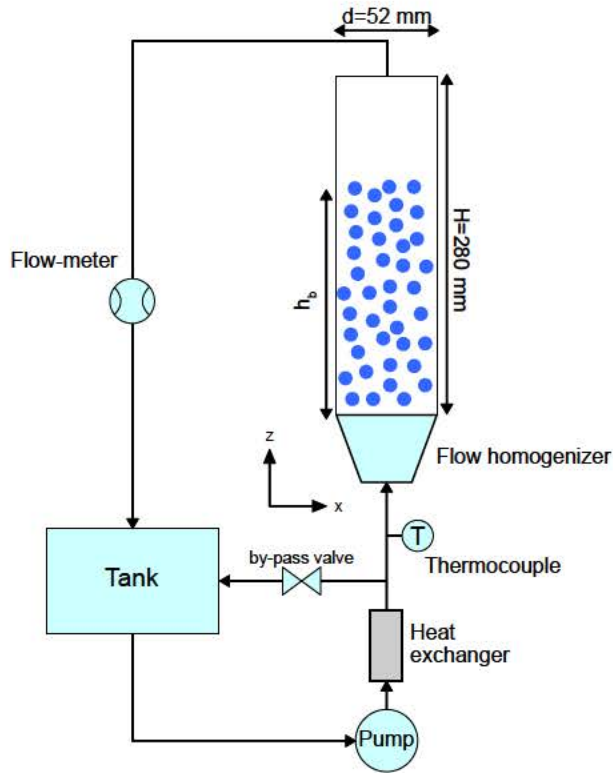


FIG. 1. Schematic of the fluidization column



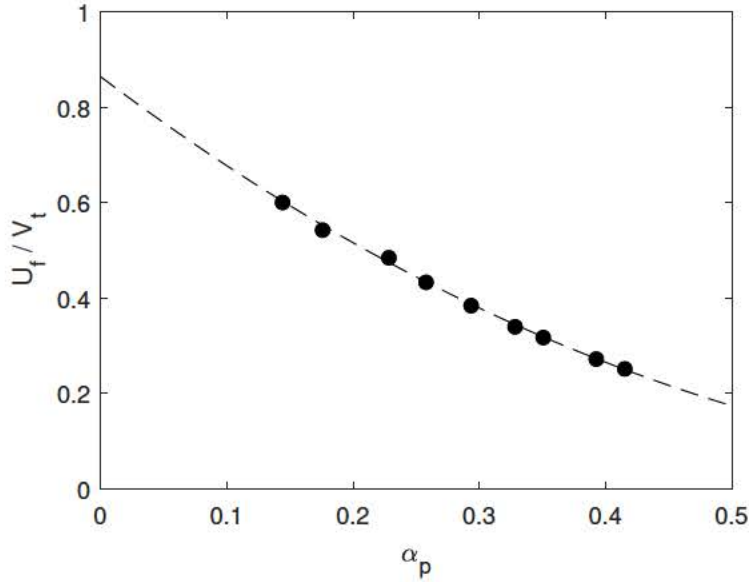


FIG. 2. Fluidization velocity  $U_f$  normalized by the particle terminal velocity  $V_t$  as a function of the particle volume fraction  $\alpha_p$ . Circles: measurements obtained from bed elevation. Dashed line: fluidization law,  $U_f/U_0 = (1 - \alpha_p)^n$ , with  $U_0 = 0.19$  m/s and  $n = 2.31$ .

### B. Flow regime and fluidization law

The terminal velocity  $V_t$  of an isolated particle has been found equal to 0.22 m/s. It is close to the value predicted for a sphere by the Schiller & Naumann correlation [23], suggesting that the small departure from sphericity of the particle shape can be disregarded. The Reynolds and Stokes numbers of an isolated particle are respectively  $Re_t = \frac{\rho_l V_t d}{\mu} = 530$  and  $St = \frac{8\rho_p}{3\rho_l C_D} = 7$ , where  $C_D$  is the drag coefficient calculated from Schiller & Naumann correlation (Note that the classical definition of the Stokes number is recovered by replacing  $C_D$  by that of the Stokes drag). The fluidization law relates the fluidization velocity  $U_f = \frac{4Q}{\pi D^2}$  (where  $D$  is the diameter of the column and  $Q$  the liquid flow rate) to the global particle volume fraction in the bed. The volume fraction is experimentally determined from the measurement of bed elevation  $h_b$ :  $\alpha_p = \frac{4m_p}{\rho_p h_b \pi d^2}$ , where  $m_p$  is the mass of particles introduced in the column. The height of the unexpanded bed is 5.7 cm and its volume fraction is 0.64. The volume fraction  $\alpha_p$  is varied from 0.14 to 0.42 by changing  $h_b$  from 26 cm to 8.7 cm. This experimental configuration corresponds to a stable homogeneous fluidized bed in the inertial regime with a moderate effect of collisions.

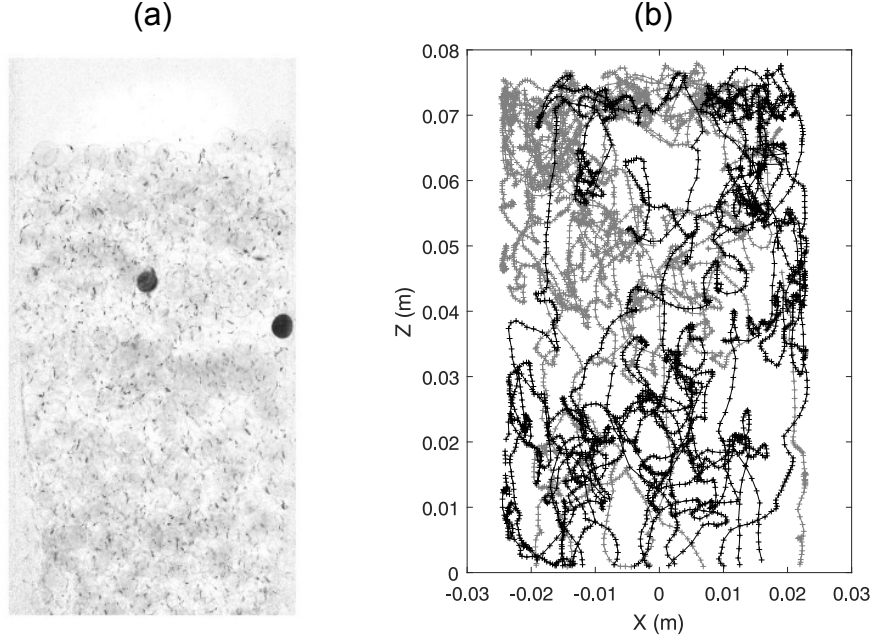


FIG. 3. Particle tracking in the fluidized bed with matched refractive indices ( $\alpha_p = 35\%$ ). (a) Snapshot of the bed where two tagged particles are present. (b) Trajectories of the two tagged particles.

Figure 2 shows the evolution of the fluidization velocity  $U_f$  as a function of the particle volume fraction. It is well described by the following empirical law,

$$U_f = U_0(1 - \alpha_p)^n, \quad (3)$$

where  $U_0 = 0.19\text{m/s}$  is close to  $V_t$  and  $n = 2.31$ . This result is consistent with Richardson-Zaki's correlation, which proposes  $n = 4.4Re_p^{-0.1} = 2.35$ .

### III. MEASUREMENT TECHNIQUES

This section describes the non-intrusive optical measurement techniques that are implemented thanks to the matching of the optical indices of the two phases.

#### A. Solid-phase characterization

The motion of the particles is characterized by means of two-dimensional particle trajectory. It consists in tagging one or two particles in black and following their trajectory

through the bed. For that purpose, a camera (Miro Lab 320), equipped with a 60 mm lens, records the successive locations of each tagged particle in the  $(x,z)$  plane with an integration time of 250  $\mu\text{s}$  and an acquisition rate of 40 Hz, which corresponds to a maximum particle displacement between two successive images of less than one diameter. Opposite to the camera, is placed a white LED panel that ensures a uniform background illumination of the image field. A typical image of two marked particles in the bed is displayed in figure 3a.

The center of mass of each tagged particle is detected thanks to an image processing technique based on a thresholding method. First, the lighting inhomogeneities of the LED panel are attenuated by normalizing each image with a background image. Then, a threshold is performed to binarize the image and detect the darkest pixels. Only objects the size of which is close to the particle diameter are finally retained. In that way, only tagged particles are detected and the position of their center can be localized at each time step. Figure 3b displays typical trajectories of the center of two tagged particles within the fluidized bed. The instantaneous velocity components  $v_x$  and  $v_z$  of each particle are then determined along its trajectory by simply dividing the displacement between two images by the time step. This leads to an accuracy on the velocity better than 0.02 cm/s. Then, the statistics of particle velocity fluctuations are computed from data collected on a few trajectories corresponding to an overall time duration of at least 5 min, which was checked to be enough to ensure good convergence.

## B. Liquid-phase characterization

Planar particle image velocimetry (PIV) is used to determine the liquid velocity field in the  $(x,z)$  plane. The flow is seeded with red-fluorescent polystyrene tracers (PS-FluoRed-Fi227, Microparticles GmbH) of diameter  $d_{PIV} = 48.2 \pm 0.6 \mu\text{m}$  and density 1050 kg/m<sup>3</sup>. A Nd:YAG laser (Litron Lasers nanoPIV, 2×120 mJ, 532 nm) generates a vertical sheet of light parallel to the  $(x,z)$  plane of maximal thickness  $w_l \approx 0.5$  mm. A camera (Lavision Imager pro), equipped with a 50 mm lens, is synchronized with the laser pulses and records images of the fluorescent tracers. The image field area is  $52.8 \times 52.8 \text{ mm}^2$  with a resolution of 22.73 pixel/mm and is located about 8 cm above the bottom of the column.

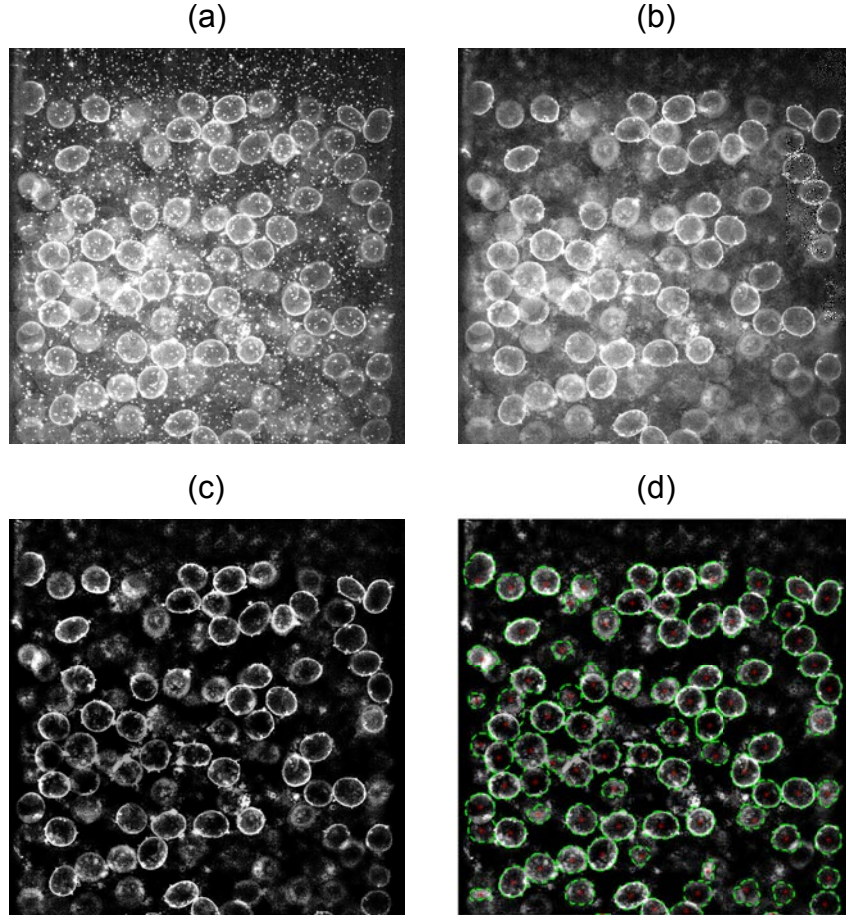


FIG. 4. Image processing for particle detection ( $\alpha_p = 35\%$ ). (a) Raw PIV image. (b) Filtering of PIV particles. (c) Correction of background inhomogeneity. (d) Determination of particle contours (green dashed lines) and centers (red stars).

Figure 4(a) shows an example of a raw image obtained with the PIV setup. We see that the Nafion particles fluoresce in the same range of wavelength as the PIV tracers. We therefore need to discriminate the particles constituting the dispersed phase from the PIV tracers before the computation of the velocity field. A three-step image processing has been developed in order to mask the Nafion particles. PIV tracers are first filtered by using an adaptative threshold using a kernel of  $28 \times d_{PIV}$  width and by filling the elements smaller than  $166 \times d_{PIV}^2$  with the value of the pixels that surround them (figure 4b). Then, background inhomogeneities are smoothed out by subtracting an instantaneous background image to the current image, which enhances the grey-level gradients at the particle surface

(figure 4c). This background image is obtained by the application of a median filter with a kernel of  $1.11 \times d_p$  width. Then, the cleaned image is binarized by applying an adaptive threshold (again with a kernel of  $1.11 \times d_p$  width) and the contours of the Nafion particles (green dashed lines in figure 4d) are closed by combining a dilatation over four pixels and equivalent circles. Finally, the interior of these contours are filled with zeros to generate the mask.

Once Nafion particles have been masked, an instantaneous velocity field is calculated each  $1/9$  s from a pair of images separated by a time step of 1 ms. The computation is carried out by Davis 8.4 PIV software developed by Lavisio, which is based on a multi-pass cross-correlation algorithm. Interrogation windows of  $32 \times 32$  pixels with a 50% overlap are used, in combination with a median filter. For each operating condition, 1500 uncorrelated velocity fields have been recorded, ensuring a good convergence in the estimation of the statistical properties.

Two global quantities are evaluated for validation purposes. The global particle volume fraction determined from the bed elevation is compared with that derived from the time-averaged surface fraction of the mask of Nafion particles. The relative difference between these two quantities is found to be less than 7%, whatever the fluidization velocity. In addition, the average liquid vertical velocity determined from PIV measurements is compared to  $U_f/(1 - \alpha_p)$ , where the fluidization velocity  $U_f$  is determined by means of a flowmeter. On average, the discrepancy between the two values is always below 10 %, which is reasonably small for PIV measurements in a dense dispersed flow.

#### IV. EXPERIMENTAL RESULTS

This section is devoted to the presentation of the experimental results, starting with the spatial distribution of the particles, before addressing the velocity statistics of the liquid and the particles.

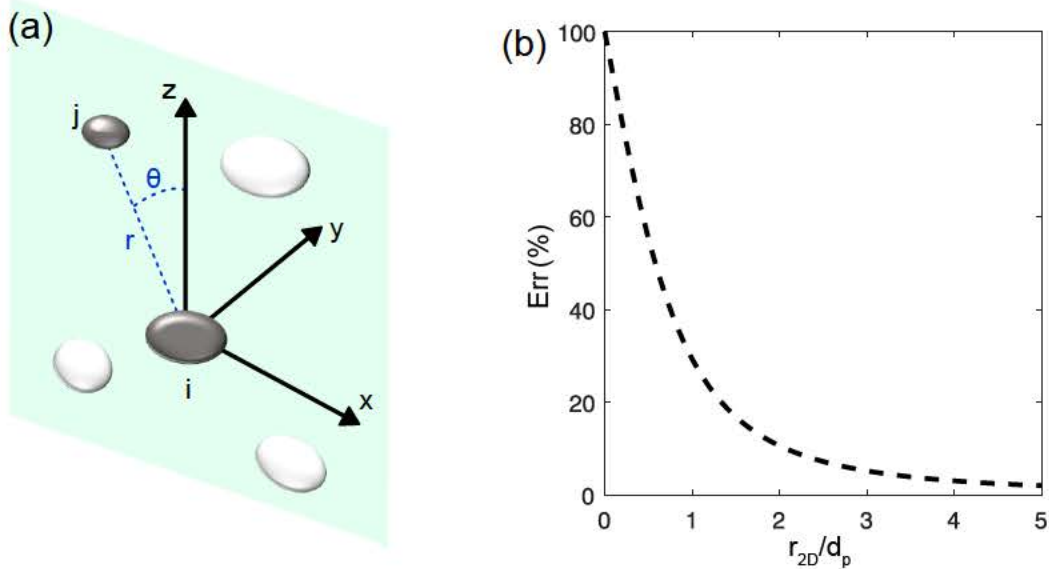


FIG. 5. Definitions and source of uncertainty regarding the determination of the pair distribution functions of the particles. (a) Frame definition for functions  $G_r$  and  $G_\theta$ . (b) Maximum relative error on inter-particle distance as a function of the normalized distance.

### A. Spatial distribution of the particles

The spatial distribution of the particles is assessed by examining their pair distribution functions. We start by considering the radial pair distribution  $G_r(r)$ , which is the probability density for a particle  $j$  to be located at a distance  $r$  from a particle  $i$  (figure 5a). By definition,  $G_r(r) = 1$  when particle locations are uniformly distributed and independent of each other, whereas  $G_r(r) > 1$  corresponds to an excess of particles at a distance  $r$ .

The first step in the experimental determination of  $G_r$  is the detection of the center of each particle belonging to the PIV measurement plane. This is carried out by performing a watershed segmentation of the contours detected during the building of the mask of solid particles on PIV images (see section III B and figure 4d). From that, we obtain the coordinates  $(x_i, z_i)$  of the center of each particle  $i$  that intersects the laser sheet. However, the laser sheet having a finite thickness  $w_l$ , the coordinates  $y_i$  of the particle centers are unknown and the distance between two detected particles in the  $y$ -direction ranges between 0 and  $d_p + w_l$ . Consequently, the inter-particle distance  $r_{2D}$  calculated by assuming that all particle centers lie in the same  $(x, z)$  plane is slightly underestimated compared to the real three-dimensional

distance  $r$ . The maximum relative error on  $r_{2D}$  caused by the uncertainty in the y-location of the particle centers is a function of  $r_{2D}/d_p$  and writes

$$Err(r_{2D}) = \frac{\{1 + (\frac{r_{2D}}{d_p})^{-2}[1 + (w_l/d_p)]^2\}^{1/2} - 1}{\{1 + (\frac{r_{2D}}{d_p})^{-2}[1 + (w_l/d_p)]^2\}^{1/2}}. \quad (4)$$

As shown in figure 5b,  $Err(r_{2D})$  decreases rapidly towards zero with the inter-particle distance: it is 30% at  $d_p$  and drops under 10% at  $2d_p$ . In the following, all calculations are based on the two-dimensional distance  $r_{2D}$ , which will be written  $r$  for sake of simplicity.

The radial pair density  $G_r$  is computed by counting the number of particles  $j$  located at a distance  $r_{ij}$  in between  $r - \Delta r$  and  $r + \Delta r$  of all particles  $i$  located in a disk of radius  $R$  having its center in the middle of the image [24]:

$$G_r(r) = \frac{\pi R^2}{N_b} \frac{1}{2\pi r \Delta r (N_b - 1)} \sum_{i=1}^{N_b} \sum_{j \neq i} [\mathcal{H}(r_{ij} - r + \Delta r) - \mathcal{H}(r_{ij} - r - \Delta r)], \quad (5)$$

where  $N_b$  is the total number of particles present in the disk of radius  $R$  and  $\mathcal{H}$  is the Heaviside function which is equal to 0 for  $x < 0$  and 1 otherwise. In most cases, the radial step  $\Delta r$  is taken equal to  $0.1 \times d_p$  and the radius  $R$  of the region of interest to  $H_f/6$ , where  $H_f = 52.8$  mm is the height of the field of view. However, for  $\alpha_p = 0.14$  and  $\alpha_p = 0.42$ ,  $R$  is taken respectively equal to  $H_f/5$  and  $H_f/4$ , in order to increase statistical convergence. In all cases, the number  $N_b$  of particles is greater than 5000, which ensures a satisfactory statistical convergence.

Figure 6 displays the experimental radial pair distribution function  $G_r(r/d_p)$  for different volume fractions. The peak around  $r/d_p = 1$ , as well as the non-zero values observed for  $r/d_p < 1$ , are due to the finite thickness of the laser sheet used to light the particles, as discussed above. For  $r/d_p > 1.5$ , the measurements are reliable and  $G_r$  is unity, indicating a uniform distribution of the inter-particle distances.

We now examine the angular distribution of the particles by considering the angular pair distribution  $G_\theta(\theta)$ , which is defined here as the probability density that the separation vector between two particles at a distance  $r$  in between  $1.5d_p$  and  $2.5d_p$  makes an angle  $\theta$  with the vertical direction.  $G_\theta(\theta)$  is plotted in figure 7 for various solid fractions. The particles display a slight preferential alignment in the horizontal direction ( $\theta = 90$  deg), which tends to disappear as  $\alpha_p$  is increases. A similar trend of horizontal clustering was observed in large Reynolds-number bubble swarms [24, 25] for gas volume fractions lower than 15%

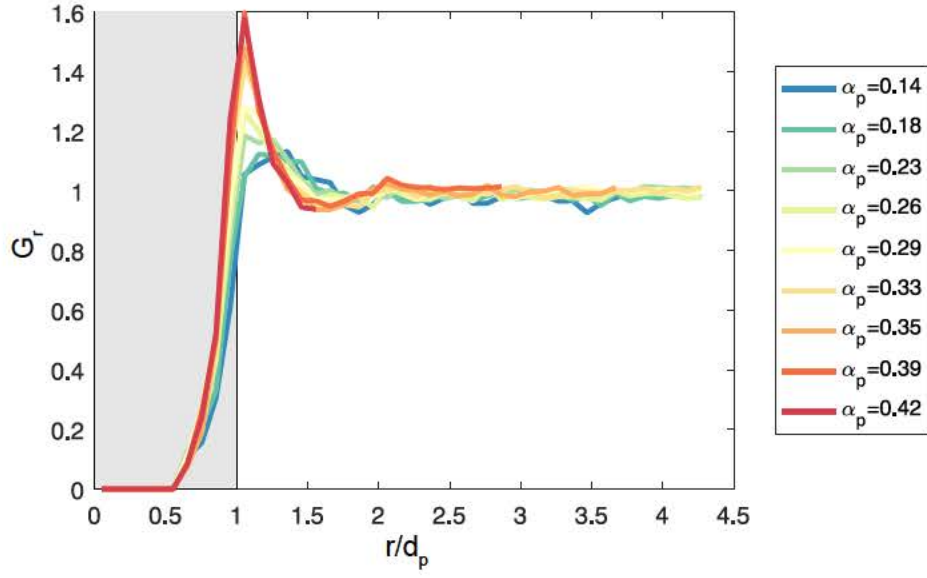


FIG. 6. Radial pair distribution function  $G_r$  of the particles as a function of the normalized distance  $r/d_p$ , for various solid fractions.

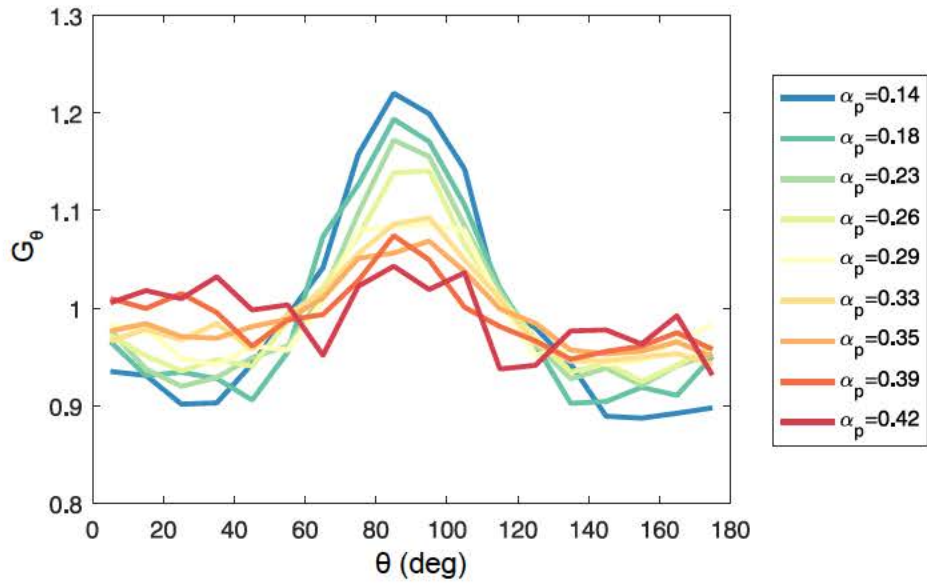


FIG. 7. Angular pair distribution  $G_\theta$  of particles located at a distance  $r$  in between  $1.5d_p$  and  $2.5d_p$  of another particle, for various particle volume fractions ( $\theta=90$  deg corresponds to a horizontal alignment).



and attributed to the fact that the stable position of two rising bubbles corresponds to a horizontal alignment, in particular because of the lift force that drives a bubble out of the wake of the one that precedes it [26].

### B. Statistics of the liquid-velocity fluctuations

Figure 8 shows the standard deviations of the two components of the liquid velocity, normalized by the mean liquid velocity  $\langle U_z \rangle = U_f/(1 - \alpha_p)$ , as a function of the particle volume fraction. Both components are growing functions of  $\alpha_p$ , which are well described by eq 1, with a constant anisotropy ratio  $\gamma_z/\gamma_x$  equal to 1.56.

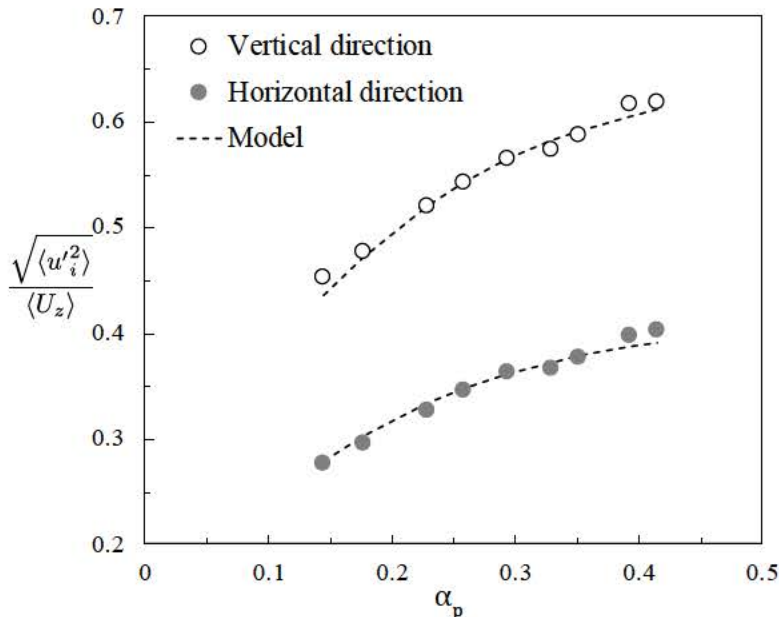


FIG. 8. Standard deviations of the two components of the liquid velocity as a function of  $\alpha_p$ . Symbols: experimental data. Dotted lines: model predictions from equation 1 with  $\gamma_z = 1.24$  and  $\gamma_x = 0.79$ .

Figure 9 displays semilog plots the p.d.f.s of the fluctuations the liquid velocity normalized by their standard deviation. In the horizontal direction, the p.d.f.s of all volume fractions collapse on a single curve, which is symmetric and non-Gaussian, showing exponential tails on both sides. Vertical p.d.f.s are asymmetric and their asymmetry evolves with the volume fraction. It even reverses at a certain value  $\alpha_{pc} = 0.26$ , showing an exponential tail on the

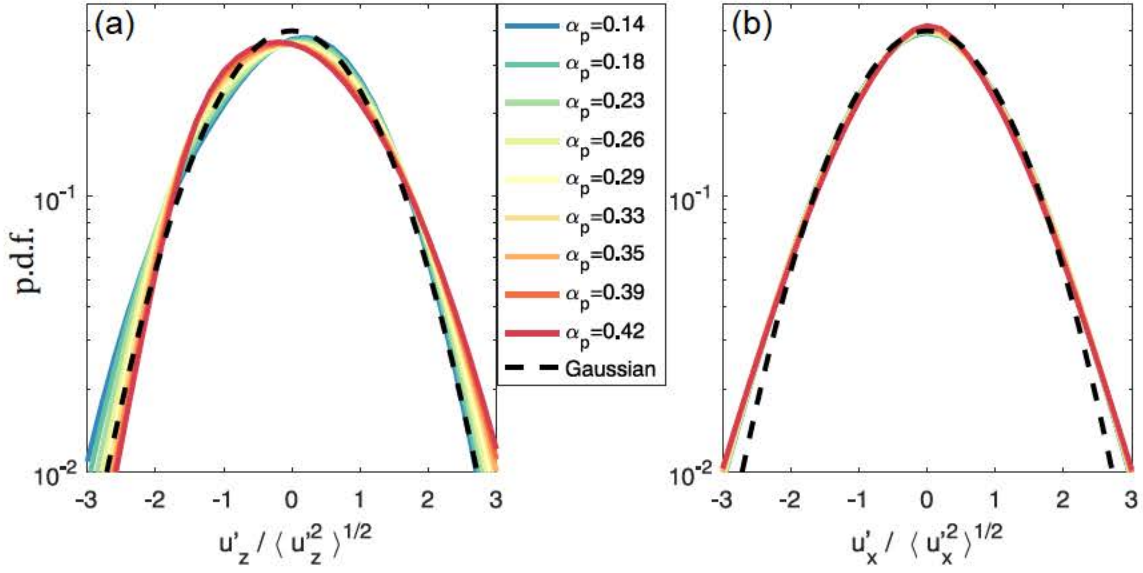


FIG. 9. Probability density functions of the liquid velocity fluctuations normalized by their standard deviation. (a) vertical component. (b) horizontal component.

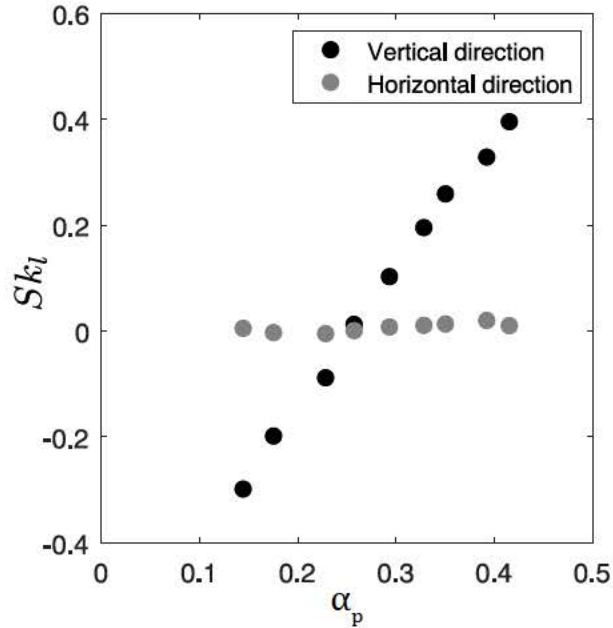


FIG. 10. Skewness coefficients of the two components of the liquid velocity as a function of  $\alpha_p$

left side for  $\alpha_p < \alpha_{pc}$  and on the right side for  $\alpha_p > \alpha_{pc}$ . The level of asymmetry can be

quantified by considering the skewness coefficient,  $Sk_{l_i} = \langle u_i^3 \rangle / \sqrt{\langle u_i^2 \rangle}^3$ , which is plotted in figure 10. While the horizontal skewness,  $Sk_{l_x}$ , remains null over the whole range of  $\alpha_p$ , the vertical one,  $Sk_{l_z}$ , monotonously increases with  $\alpha_p$ . It starts from significant negative values ( $Sk_{l_z} = -0.3$  at  $\alpha_p = 0.14$ ), cancels at the same value  $\alpha_{pc} = 0.26$  previously determined in fig 9 from the p.d.f.s, to finally reaches large positive values ( $Sk_{l_z} = 0.42$  at  $\alpha_p = 0.42$ ).

### C. Statistics of the particle-velocity fluctuations

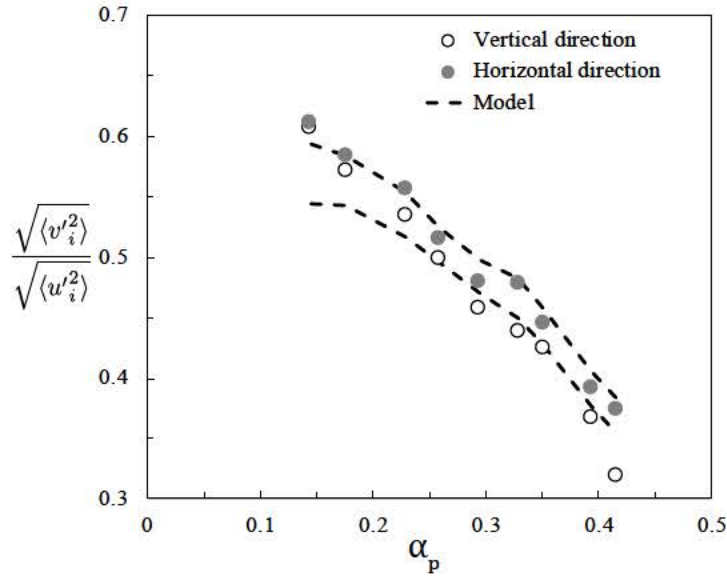


FIG. 11. Ratio between the standard deviations of the particle and the liquid velocities as a function of  $\alpha_p$ . Symbols: experiments. Dotted lines: model predictions from eq 2 with  $k_x = 0.21$  and  $k_z = 0.35$ , calculated by using experimental values of  $\sqrt{\langle u_i^2 \rangle}$

Figure 11 shows the ratio of the standard deviation of the particle velocity  $\sqrt{\langle v_i^2 \rangle}$  and that of the liquid velocity  $\sqrt{\langle u_i^2 \rangle}$  as a function of  $\alpha_p$ . For both components, this ratio is always smaller than unity, indicating that particles are filtering the liquid fluctuations. By extrapolating toward the dilute regime, the results seem in good agreement with the Tchen-Hinze theory, which predicts a value of this ratio close to 0.75 for the present system at  $\alpha_p = 0$  (see [22]). Then, increasing  $\alpha_p$ , the particle-to-fluid fluctuation ratio decreases steeply, which shows that the filtering is strongly enhanced by the concentration. This effect

is well reproduced by the model proposed in [22] and given by equation (2).

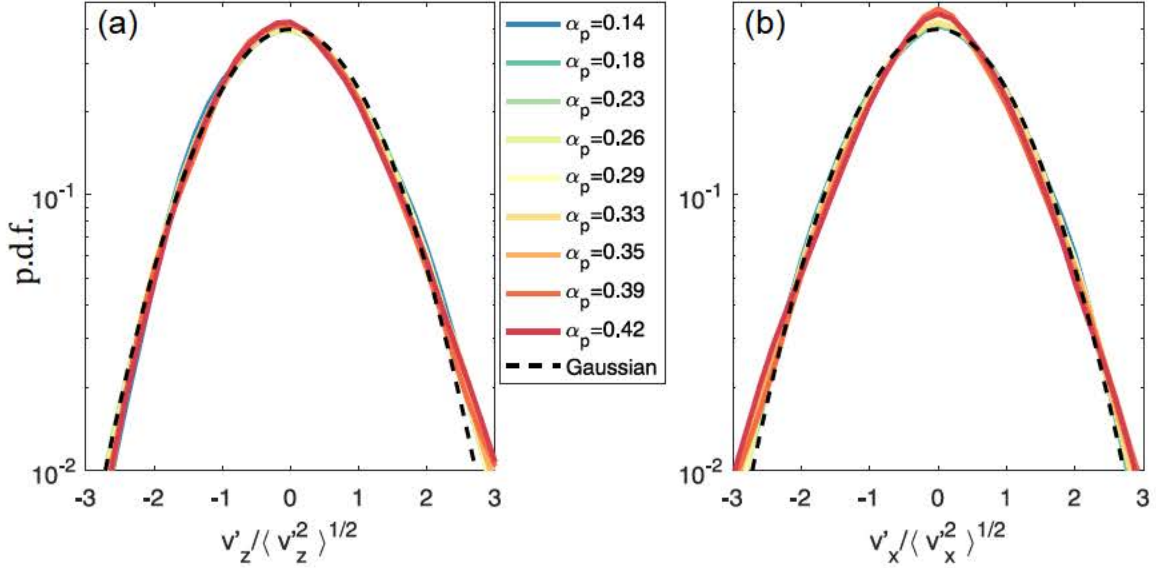


FIG. 12. Probability density functions of the particle velocity fluctuations normalized by their standard deviation. (a) vertical component. (b) horizontal component.

Figure 12 displays the p.d.f.s of the two components of the particle velocity fluctuations normalized by their own standard deviation, for various particle volume fractions. The p.d.f.s are again non-Gaussian, symmetric in the horizontal direction with exponential tails on both sides, and asymmetric in the vertical direction with an exponential tail in the upwards direction. In the horizontal direction, we also note the presence of a peak around the origin, the amplitude of which increases with  $\alpha_p$ . This peak has already been observed by Aguilar et al. [20], who attributed it to a possible signature of inelastic collisions between particles, which generates more and more zero-velocity events as the solid fraction increases.

The skewness coefficients of the particle fluctuations are shown in figure 13. As expected, the horizontal one is null. More surprisingly, the vertical one is always positive:  $Sk_{p_z}$  keeps a constant value close to 0.17 for  $\alpha_p \leq 0.3$  and then monotonously increases at larger particle volume fractions, up to reach 0.31 at  $\alpha_p=0.42$ . Comparing particles to liquid,  $Sk_{p_z}$  and  $Sk_{l_z}$  thus experiences a transition around approximately the same value of  $\alpha_p$ , but while their values are close at large concentrations, they strongly differ at lower ones.

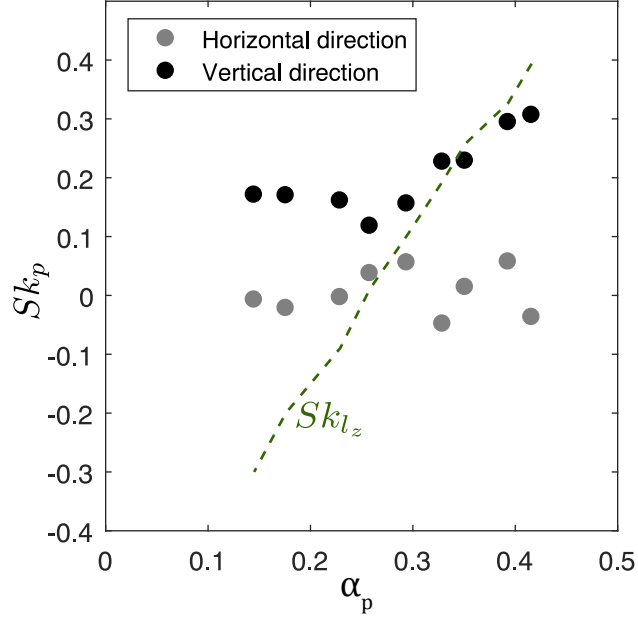


FIG. 13. Skewness coefficients of the two components of the particle velocity as a function of  $\alpha_p$ . (The dashed line shows the skewness  $Sk_{l_z}$  of the vertical fluid velocity).

## V. PHYSICAL INTERPRETATION AND MODELING

In a previous rapid communication [22], we have proposed to subdivide the liquid volume into a wake region and an interstitial region. This allowed us to derive models of the variances of the liquid and particle velocities, the mathematical expressions of which are recalled by eqs 1 and 2. Now, we propose to develop this concept to build a model for the probability density functions of the velocity fluctuations. Since the variances have already been modelled, we focus on the p.d.f.s of the normalized fluctuations of the liquid  $u_i^* = u_i' / \sqrt{u_i'^2}$  and of the particle  $v_i^* = v_i' / \sqrt{v_i'^2}$ . We consider first the liquid phase before dealing with the particles.

### A. Liquid-velocity p.d.f.s

Figure 14 schematizes the liquid flow by considering that it is divided into two separate regions: (1) the wake region  $\mathcal{W}$  wherein vertical fluctuations are negative due to the entrainment of the liquid by the particles and (2) the interstitial region  $\mathcal{I}$  where it is the reverse ( $u_z^* > 0$ ) since the average of the fluctuations over the whole volume of liquid is null

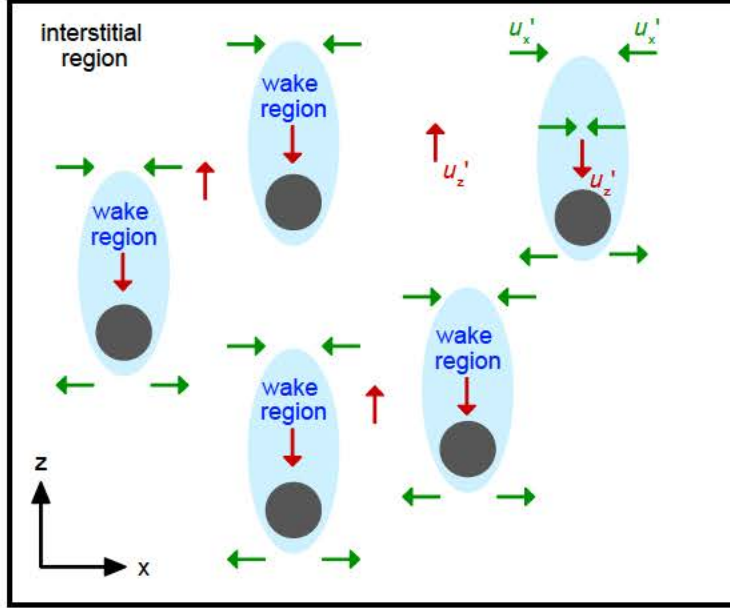


FIG. 14. Definitions of the two regions within the liquid phase of a fluidized bed.

$(\langle u'_z \rangle = 0)$ .

At low  $\alpha_p$ , the volume  $\mathcal{V}_W$  of the wake region is small whereas the volume  $\mathcal{V}_I$  of the interstitial region is large. Therefore, the negative vertical fluctuations due to the wakes are rare, but of large magnitude compared to the reverse flow within the interstices. As it has been demonstrated in [27], this generates an exponential tail on the left side of the p.d.f. of the vertical velocity, which corresponds to the direction of the wake-induced flow. On the other hand, positive vertical fluctuations located in the interstitial region are less intense and smoothly distributed over a large volume, so they do not give birth to an exponential tail on the right side of the p.d.f. Thus, we understand why the experimental p.d.f.s of the vertical liquid velocity fluctuations,  $f_{lz}(u'_z)$ , are asymmetric with an exponential tail on the left side and a Gaussian shape on the right side.

Increasing  $\alpha_p$ , the interstitial volume decreases, so that  $\mathcal{V}_W$  ends up becoming larger than  $\mathcal{V}_I$ . At large  $\alpha_p$ , vertical fluctuations of large magnitude are thus located within the interstitial region. The situation is thus reversed compared to the case at low  $\alpha_p$ . Strong interstitial fluctuations are positive and rare, while negative fluctuations within wakes remain moderate. The probability density  $f_{lz}(u'_z)$  therefore exhibits a Gaussian behavior on the left side and an exponential tail on the right side.

Let us define  $f_{l_z}^{low}(u_z^*)$  as the p.d.f. of vertical velocity fluctuations of the lowest possible value  $\alpha_p^{low}$  of the volume fraction, which generally corresponds to the largest fluidization velocity ensuring a stable homogeneous fluidized bed. We also define  $f_{l_z}^{high}(u_z^*)$  as the p.d.f. of the largest possible volume fraction  $\alpha_p^{high}$ , which corresponds to the lower liquid velocity allowing the fluidization of the particles. The experiments show that  $f_{l_z}(u_z^*)$  smoothly evolves from  $f_{l_z}^{low}(u_z^*)$  to  $f_{l_z}^{high}(u_z^*)$  as  $\alpha_p$  increases (fig 9). A simple model of  $f_{l_z}(u_z^*)$  can thus be obtained by considering  $f_{l_z}(u_z^*)$  as a linear combination of the p.d.f.s. of the two extreme cases,

$$f_{l_z}(u_z^*) = (1 - \Phi)f_{l_z}^{low}(u_z^*) + \Phi f_{l_z}^{high}(u_z^*). \quad (6)$$

The weighting parameter  $\Phi$  ranges between 0 and 1. It characterizes the proportion of intense negative fluctuations, while  $1 - \Phi$  characterizes that of intense positive fluctuations. It is an increasing function of the wake volume fraction,  $\mathcal{V}_w^* = \mathcal{V}_W/(\mathcal{V}_W + \mathcal{V}_I)$ , which is itself an increasing function of the particle volume fraction  $\alpha_p$ . It has to be equal to 1/2 at  $\alpha_p = \alpha_{pc}$ , where the wake volume is equal to the interstice volume and the distribution is symmetric. Assuming a linear increase of  $\Phi$  with  $\alpha_p$ , we get

$$\Phi = \frac{1}{2} + k_\Phi(\alpha_p - \alpha_{pc}), \quad (7)$$

where the prefactor  $k_\Phi$  should be greater than unity, since  $\Phi$  is expected to pass from almost zero to one while  $\alpha_p$  increases from  $\alpha_p^{low} > 0$  to  $\alpha_p^{high} < 1$ . Knowing that they have skewnesses of opposite signs and that  $f_{l_z}^{low}$  is symmetric at  $\Phi(\alpha_{pc}) = 0.5$ , eqs. 6 and 7 require that  $f_{l_z}^{low}$  and  $f_{l_z}^{high}$  are symmetric with respect to the ordinate axis,

$$f_{l_z}^{high}(u_z^*) = f_{l_z}^{low}(-u_z^*) = f^{ref}(u_z^*). \quad (8)$$

With a few assumptions, we thus end up with the model defined by eqs. 6-8, which involves two scalar parameters,  $\alpha_{pc}$  and  $k_\Phi$ , and a single centred normalized p.d.f.,  $f^{ref}(u_z^*)$ , that is independent of  $\alpha_p$  and can be described by a Gaussian distribution to which an exponential tail is added on the right side. Note that  $f_{l_z}^{low}$  and  $f_{l_z}^{high}$  are p.d.f.s of zero average and unit variance, hence  $f^{ref}$  is as well. We have now to check whether this model is in agreement with the experiments.

Figure 15b displays the experimental p.d.f.s  $f_{l_z}^{low}(-u_z^*)$  measured at  $\alpha_p^{low} = 0.14$  and  $f_{l_z}^{high}(u_z^*)$  at  $\alpha_p^{high} = 0.42$ . We observe that  $f_{l_z}^{low}(-u_z^*)$  and  $f_{l_z}^{high}(u_z^*)$  match very well, which

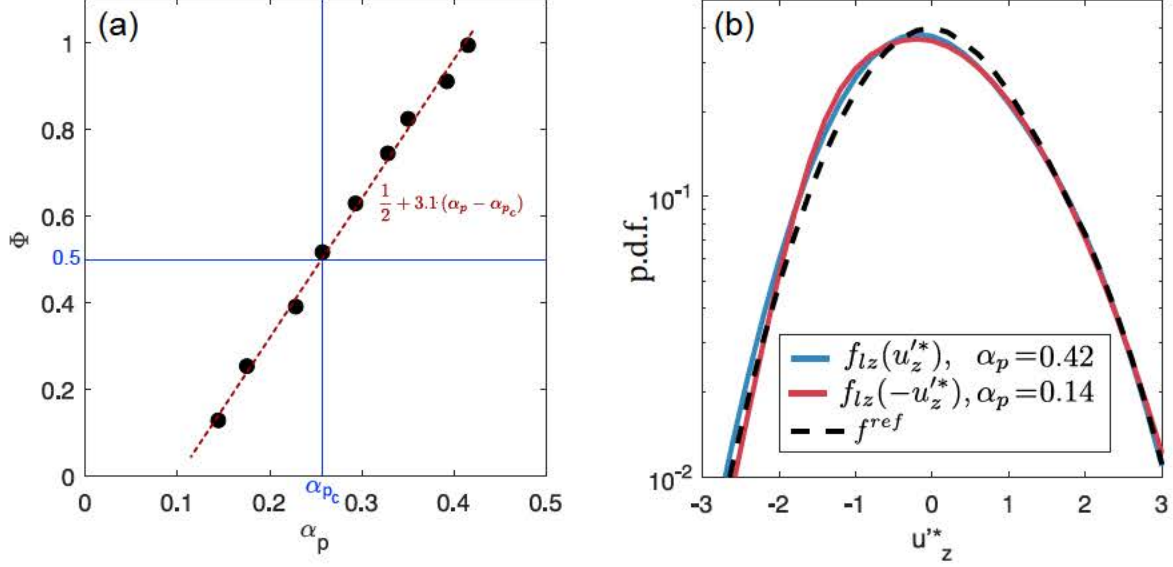


FIG. 15. Modeling of liquid fluctuations. (a) weighting parameter  $\Phi$ . (b) p.d.f.s of velocity fluctuations at low ( $f_{lz}^{low}$ ) and large ( $f_{lz}^{high}$ ) particle volume fractions for the determination of the reference distribution  $f^{ref}$ .

confirms the symmetry assumption expressed by eq 8. We can then search for an analytical expression of  $f^{ref}(u_z^*)$ . To that aim, we introduce a Gaussian distribution,

$$f_1^{ref}(\xi) = \frac{1}{2\pi} \exp\left(-\frac{\xi^2}{2}\right), \quad (9)$$

and an exponential tail,

$$\begin{aligned} f_2^{ref}(\xi) &= 0 \quad \text{for } \xi < 2, \\ f_2^{ref}(\xi) &= \frac{1}{\nu} \exp\left(-\frac{\xi}{\nu}\right) \quad \text{for } \xi \geq 2, \end{aligned} \quad (10)$$

and add them together

$$f_{raw}^{ref}(\xi) = f_1^{ref}(\xi) + f_2^{ref}(\xi). \quad (11)$$

This distribution has a non-zero mean  $M_{raw}$  and a non-unit standard deviation  $\sigma_{raw}$ . A centred normalized distribution is then obtained by

$$f^{ref}(\xi) = \sigma_{raw} f_{raw}^{ref}(\sigma_{raw} \xi + M_{ref}). \quad (12)$$

Fig 15b shows that function  $f^{ref}(u_z^*)$  given by eq 12 with  $\nu=0.46$  is a reasonable fit of the experimental results.



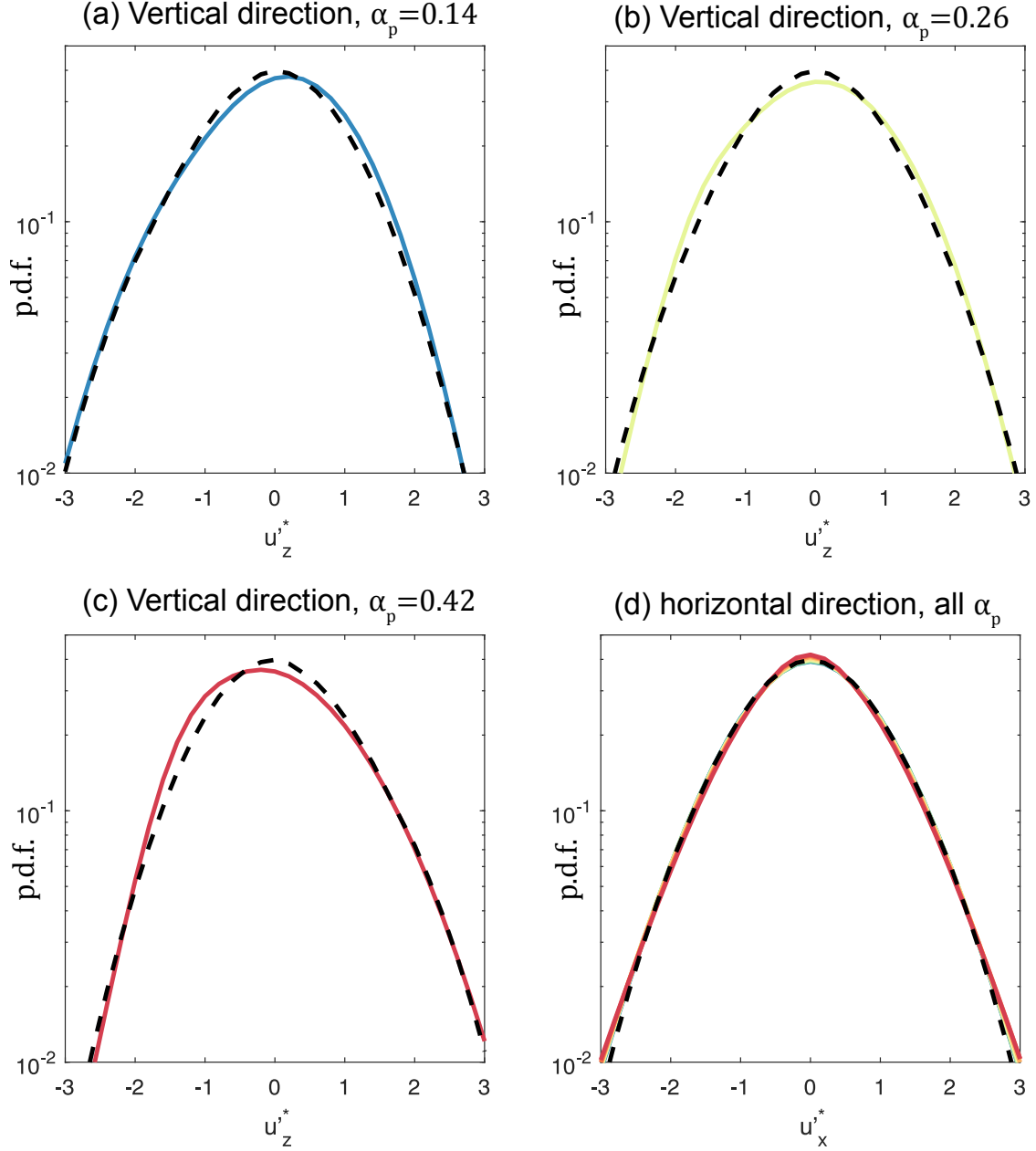


FIG. 16. Comparison between model and experimental p.d.f.s. for the liquid. Black dashed lines: model. Colored lines: experiments.

Then, we need to determine  $\Phi(\alpha_p)$ . Using eqs 6 and 8, the skewness coefficient of the liquid vertical velocity writes

$$Sk_{l_z} = \int_{-\infty}^{+\infty} \xi^3 f_{l_z}(\xi) d\xi = (2\Phi - 1) \int_{-\infty}^{+\infty} \xi^3 f^{ref}(\xi) d\xi. \quad (13)$$

Performing the summation with the experimentally fitted function  $f^{ref}(\xi)$ , we find  $\int_{-\infty}^{+\infty} \xi^3 f^{ref}(\xi) d\xi =$

0.4.  $\Phi$  is thus simply related to the skewness coefficient by

$$\Phi = \frac{1}{2} + 1.25 Sk_{l_z} . \quad (14)$$

Values of  $\Phi$ , computed by inserting experimental values of  $Sk_{l_z}$  in eq 14, are plotted in fig 15a. They are well approximated by eq 7 with  $\alpha_{pc} = 0.26$  and  $k_\Phi = 3.1$ . We note that  $\Phi(\alpha_p^{low})$  is small and  $\Phi(\alpha_p^{high})$  is almost equal to unity, which justifies the choice of these values of  $\alpha_p$  to fit extremes p.d.f.s  $f_{l_z}^{high}$  and  $f_{l_z}^{low}$ .

We have now all the ingredients to build the model p.d.f.s at all particle volume fractions. Figures 16a-c compare modelled p.d.f.s to measurements, showing that this simple model makes a good approximation of the vertical fluctuations of the liquid. Note that the model is exact up to the third order statistical moment, but only approximated regarding higher order moments, which explains the deviation close to maximum of the p.d.f. of the vertical fluctuations.

Horizontal liquid velocity fluctuations are directly associated to vertical ones by the conservation of the liquid volume. It is hence reasonable to think that their statistical distribution can be modelled in a similar way, as a function of  $f^{ref}$ . As in the vertical direction, horizontal fluctuations of large magnitude are located in wakes at small  $\alpha_p$  and in interstices at large  $\alpha_p$ . However, positive and negative horizontal fluctuations have equal probability, in both the wake and the interstitial regions. Horizontal p.d.f.  $f_{l_x}(u_x^*)$  is thus symmetric. In addition, vertical p.d.f.s at low and high  $\alpha_p$  are symmetrical to each other (eq 8). Consequently, the evolution of  $\mathcal{V}_W$  relative to  $\mathcal{V}_I$  is thus expected to have no influence on the horizontal p.d.f.s. We thus propose to model  $f_{l_x}$  as the simplest symmetric function based on  $f^{ref}$ ,

$$f_{l_x}(u_x^*) = \frac{1}{2} (f^{ref}(-u_z^*) + f^{ref}(u_z^*)) . \quad (15)$$

Figure 16d confirms that eq 15 describes very well the experimental distribution, without the need of introducing any additional parameters.

## B. Particle-velocity p.d.f.s

In [22], we assumed that instant local particle fluctuations are proportional to liquid ones, by involving a factor which depends on the particle volume fraction. This allowed us to derive a reliable model for the variance of the particle velocity (eq 2). Regarding the

whole statistical distribution, this assumption leads us to consider that the p.d.f.s of the particle fluctuations must be expressed in a similar way to those of the liquid, by making use of  $f^{ref}$  and of the probability  $P_p$  (resp.  $1 - P_p$ ) that the more intense fluctuations seen by the particles are negative (resp. positive). This gives, in the vertical direction,

$$f_{pz}(v_z^*) = (1 - P_p)f^{ref}(-v_z^*) + P_p f^{ref}(v_z^*), \quad (16)$$

and in the horizontal direction,

$$f_{px}(v_x^*) = \frac{1}{2} (f^{ref}(v_x^*) + f^{ref}(-v_x^*)) . \quad (17)$$

If the particles were uniformly distributed throughout the liquid volume,  $P_p$  would be equal to  $\Phi$  and the p.d.f.s of the two phases would be the same. In fact, we have seen that there is preferential horizontal alignment of the particles at lower  $\alpha_p$ , which leads the particles to avoid the wakes. As a result, intense fluctuations of negative signs are not experienced by the particles, which explains why the skewness coefficient of their fluctuations is never negative. Parameter  $P_p$  is therefore not directly related to the volume fraction of the wake and there is no obvious way to a priori relate it to  $\Phi$ . Nevertheless, it can be determined from the experimental skewness coefficient in the same manner as what has been done for the liquid phase, by means of eq 13. Figure 17 displays  $P_p$  as a function of  $\alpha_p$ . It turns out to remain roughly equal to 0.7 at  $\alpha_p \leq 0.3$  and then increases as  $2.1 \times (\alpha_p - 0.3) + 0.7$ . However, it is interesting to note that at large  $\alpha_p$ , as the particle locations become independent of each other,  $P_p$  becomes close to  $\Phi$ . Differences between particle and liquid Eulerian velocity statistics are indeed due to particle preferential concentration and do not question the proportionality between the local instant fluctuations of the two phases in the vicinity of each particle.

Inserting the values of  $P_p$  into eqs 16 and 17, we obtain the model p.d.f.s of each components of the particle velocity fluctuations and for all particle volume fractions. Figure 18 compares them to experimental ones. Except from a slight difference in the negative tail of the vertical p.d.f.s at lower  $\alpha_p$  and the central part the horizontal p.d.f.s at larger  $\alpha_p$ , the matching is satisfactory. It is remarkable that such a good agreement is obtained by making use of the same reference function  $f^{ref}$  as for the modeling of the liquid phase.

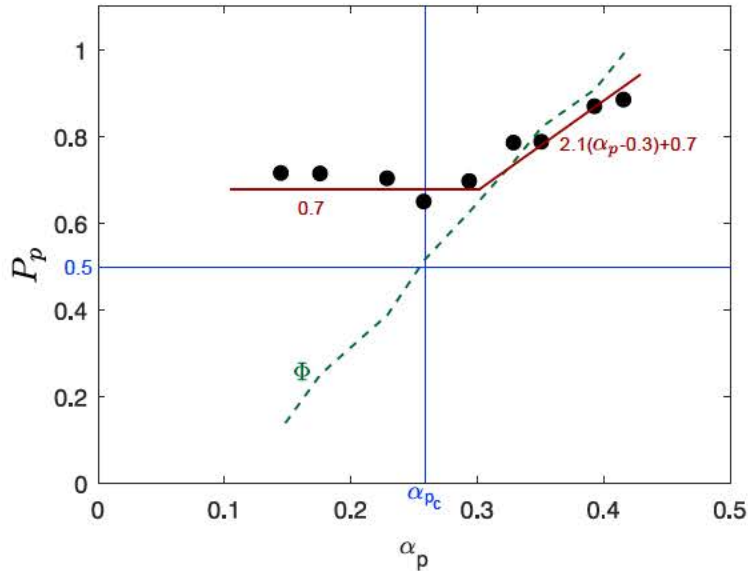


FIG. 17. Weighting parameter  $P_p$  for the particle fluctuations.

## VI. CONCLUSION

This work investigates the statistics of the velocity fluctuations in a homogeneous solid-liquid fluidized bed. Experimental results are reported for a large range of particle volume fraction ( $0.14 \leq \alpha_p \leq 0.42$ ), in a configuration at high particle Reynolds number ( $150 \leq Re_p \leq 360$ ) and moderate density ratio ( $\rho_p/\rho_l \simeq 1.5$ ). Thanks to the matching of optical indices of the liquid and the particles, the probability density functions of the velocities of both phases have been measured.

In a recent work ([22]), we proposed an interpretation of the dynamics of the velocity fluctuations based on the three following flow properties: (1) The flow is divided into a wake region where vertical liquid fluctuations,  $u'_z$ , are negative (downward) and an interstitial region where they are positive (upward); (2) Instant fluctuations of the particle velocity,  $v'_i$ , are proportional to those of the liquid,  $u'_i$ ; (3) Horizontal fluctuations,  $u'_x$  and  $v'_x$ , are similar to vertical fluctuations,  $u'_z$  and  $v'_z$ , except that their positive and negative values are symmetric. From property (1), it is deduced that instant vertical liquid fluctuations are proportional to instant fluctuations of the indicator function of the solid phase, which allows us to derive a model for the variance of the vertical liquid velocity,  $\langle u'^2_z \rangle$ . Then, using properties (2) and (3), models for the variances of the two components of the two phases

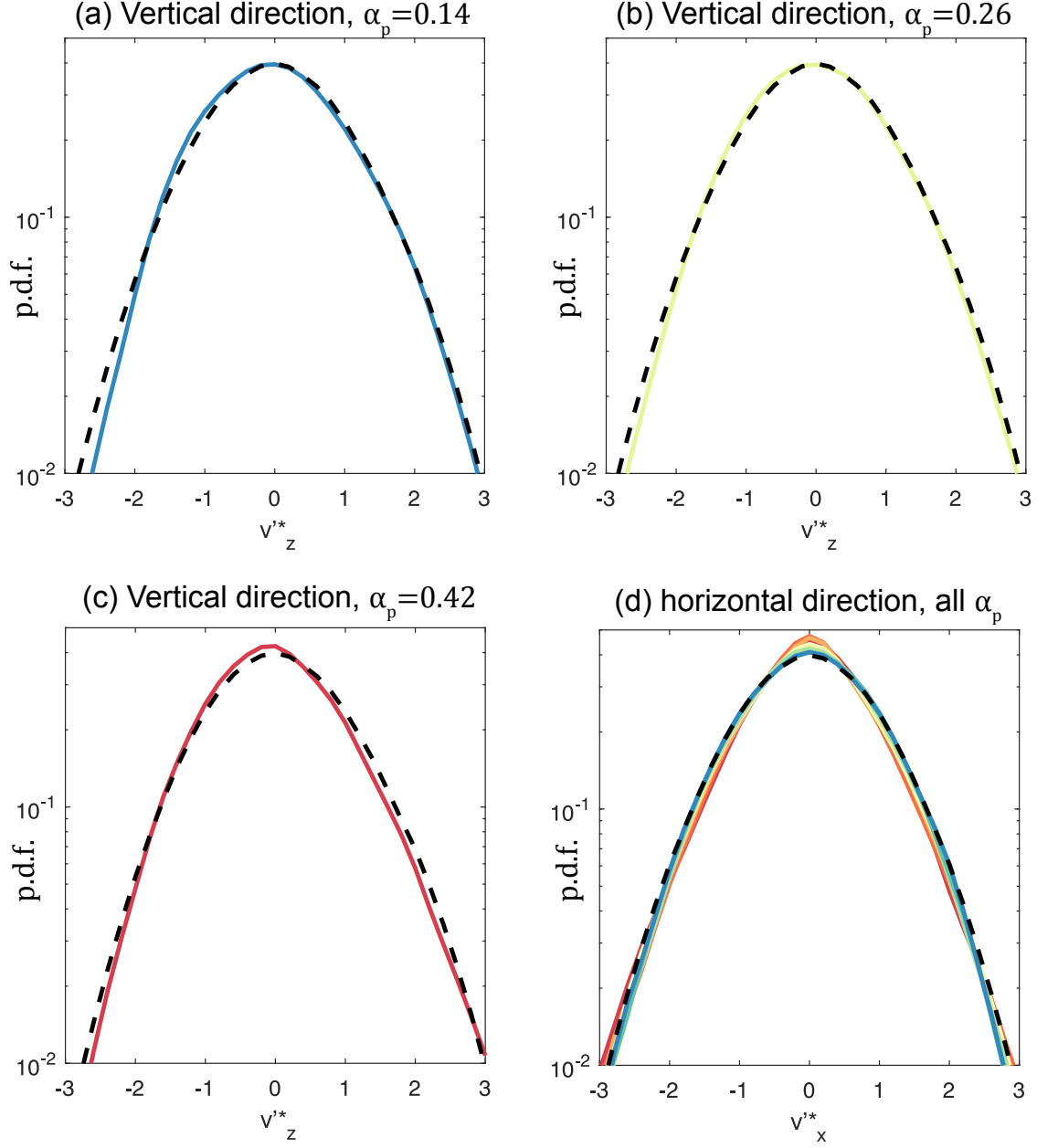


FIG. 18. Comparison between model and experimental velocity p.d.f.s. for the particles. Black dashed lines: model. Colored lines: experiments.

are obtained, which are in good agreement with experiments.

In the present work, we went further by examining the probability density functions of the velocity fluctuations. We showed that it was possible to derive a model of the normalized p.d.f.s of the fluctuations by assuming the same flow properties. Increasing  $\alpha_p$ , the relative volume of the wake region increases while that of the interstices decreases. We thus move

from a situation where negative  $u'_z$  are rare and intense while positive  $u'_z$  are common but of lower magnitude to a situation where the opposite is true. At low  $\alpha_p$ , the p.d.f.s  $f_{lz}$  of  $u'_z$  are asymmetric with a long tail on the left side and a negative skewness, whereas it is the reverse at large  $\alpha_p$ . Considering the p.d.f.s at small and large  $\alpha_p$  are symmetric, we can express  $f_{lz}$  by using a single function  $f^{ref}$  that is independent of  $\alpha_p$  (eq 8). This leads to express  $f_{lz}(u'_z)$  as a linear combination of  $f^{ref}(-u'_z)$  and  $f^{ref}(u'_z)$  (eq 6), involving a weight  $\Phi$  that characterises the relative importance of the wake and the interstices and increases with  $\alpha_p$  (eq 7). Then, using property (2), the p.d.f. of the horizontal liquid velocity fluctuations  $f_{lx}$  is also related to  $f^{ref}$  (eq 15). Finally, property (3) suggests that the p.d.f.s of the particle velocity fluctuations  $f_{pz}(v'_z)$  and  $f_{px}(v'_x)$  are similar to those of the liquid phase (eqs 16-17), except that the weighting function  $P_p(\alpha_p)$  is different from  $\Phi(\alpha_p)$  because of the preferential alignment of the particles in the horizontal direction (fig 17). We end up with a model of the p.d.f.s of the two velocity components of the two phases. This model only relies on a single reference p.d.f., which displays a long exponential tail on the right side, and two weighting parameters,  $\Phi$  for the liquid and  $P_p$  for the particles. Regarding the liquid,  $\Phi$  is an increasing affine function of  $\alpha_p$  that is equal to 1/2 at the point where  $f_{lz}$  is symmetric.  $P_p$  is only equal to  $\Phi$  when particle locations are independent of each other. In general, it has a more complex evolution which depends on the preferential concentration of the particles. This model is in good agreement with the experiments, which confirms that the dynamics of the fluctuations depicted by properties (1-3) is realistic.

Future work should consider other particle Reynolds numbers and density particle-to-fluid density ratios in order to investigate how the reference function,  $f^{ref}$ , and the weighting parameters,  $\Phi$  and  $P_p$ , vary and to determine the limits of validity of the present description.

## ACKNOWLEDGMENTS

This work has been carried out thanks to financial support of the research program AAP 2015 of Idex UNITI-BIREM conv-ANR-11-Idex-0002-02. The authors acknowledge the MESR of Région Occitanie and Toulouse Métropole (CPER 2007-2013) and Emmanuel Cid

(CNRS-INPT-UPS, LGC) for technical support.

---

- [1] N. Epstein, “Applications of liquid-Solid fluidization,” *International Journal of Chemical Reactor Engineering* **1** (2002).
- [2] F. Risso, V. Roig, Z. Amoura, G. Riboux, and A.-M. Billet, “Wake attenuation in large Reynolds number dispersed two-phase flows,” *Philosophical Transactions of the Royal Society A: Mathematical, Physical and Engineering Sciences* **366**, 2177–2190 (2008).
- [3] G. Riboux, D. Legendre, and F. Risso, “A model of bubble-induced turbulence based on large-scale wake interactions,” *Journal of Fluid Mechanics* **719**, 362–387 (2013).
- [4] Z. Amoura, C. Besnaci, F. Risso, and V. Roig, “Velocity fluctuations generated by the flow through a random array of spheres: a model of bubble-induced agitation,” *Journal of Fluid Mechanics* **823**, 592–616 (2017).
- [5] F. Risso, “Agitation, mixing, and transfers induced by bubbles,” *Annual Review of Fluid Mechanics* **50**, 25–48 (2018).
- [6] M. Mehrabadi, S. Tenneti, R. Garg, and S. Subramaniam, “Pseudo-turbulent gas-phase velocity fluctuations in homogeneous gas–solid flow: fixed particle assemblies and freely evolving suspensions,” *Journal of Fluid Mechanics* **770**, 210–246 (2015).
- [7] V. Tavanashad, A. Passalacqua, R. O. Fox, and S. Subramaniam, “Effect of density ratio on velocity fluctuations in dispersed multiphase flow from simulations of finite-size particles,” *Acta Mechanica* **230**, 469–484 (2019).
- [8] WC Moore and S Balachandar, “Lagrangian investigation of pseudo-turbulence in multiphase flow using superposable wakes,” *Physical Review Fluids* **4**, 114301 (2019).
- [9] J. Abrahamson, “Collision rates of small particles in a vigorously turbulent field,” *Chem. Eng. Sci.* **30**, 11 (1975).
- [10] G. Gouesbet, A. Berlemont, and A. Picart, “Dispersion of discrete particles by continuous turbulent motions. extensive discussion of the tchen’s theory, using a two-parameter family of lagrangian correlation functions,” *Physics of Fluids* **27**, 827–837 (1984).
- [11] E. Deutsch O. Simonin and J.P. Minier, “Eulerian prediction of the fluid/particle correlated motion in turbulent two-phase flows,” *Applied Scientific Research* **51**, 275–283 (1993).

- [12] T.B. Anderson and R. Jackson, “A fluid mechanical description of fluidized beds,” *I&EC Fund.* **6** 4, 527–539 (1967).
- [13] GK Batchelor, “A new theory of the instability of a uniform fluidized bed,” *Journal of Fluid Mechanics* **193**, 75–110 (1988).
- [14] J. Ding and D. Gidaspow, “A bubbling fluidization model using kinetic theory of granular flow,” *AIChE Journal* **36**, 523–538 (1990).
- [15] A. Boelle, G. Balzer, and O. Simonin, “Second-order prediction of the particle-phase stress tensor of inelastic spheres in simple shear dense suspensions,” *ASME-Publications-Fed* **228**, 9–18 (1995).
- [16] Yu. A. Buyevich, “Particulate stresses in dense disperse flow,” *Ind. Eng. Chem. Res.* **38**, 731–743 (1999).
- [17] P. Duru, M. Nicolas, J. Hinch and E. Guazzelli, “Constitutive laws in liquid-fluidized beds,” *Journal of Fluid Mechanics* **452**, 275–283 (2002).
- [18] E. Guazzelli and J. Hinch, “Fluctuations and instability in sedimentation,” *Annual Review of Fluid Mechanics* **43**, 97–116 (2011).
- [19] JJ Derksen and S. Sundaresan, “Direct numerical simulations of dense suspensions: wave instabilities in liquid-fluidized beds,” *Journal of Fluid Mechanics* **587**, 303–336 (2007).
- [20] A. Aguilar-Corona, O. Masbernat, R. Zenit-Camacho, and B. Figueroa-Espinoza, “Experimental and theoretical advances in fluid dynamics. environmental science and engineering.” (Springer, Berlin, Heidelberg, 2012) Chap. Agitation in a Liquid Fluidized Bed.
- [21] A. Ozel, JC de Motta Brändle, M. Abbas, P. Fede, O. Masbernat, S. Vincent, J-L Estivalezes, and O. Simonin, “Particle resolved direct numerical simulation of a liquid–solid fluidized bed: Comparison with experimental data,” *International Journal of Multiphase Flow* **89**, 228–240 (2017).
- [22] E. Alméras, O. Masbernat, F. Risso, and R. Fox, “Fluctuations in inertial dense homogeneous suspensions,” *Phys. Rev. Fluids* **4**, 102301 (2019).
- [23] R. Clift, J.R. Grace, and M.E. Weber, *Bubble, Drops and Particles* (Academic Press, 1978).
- [24] E. Bouche, V. Roig, F. Risso, and A.M. Billet, “Homogeneous swarm of high-reynolds-number bubbles rising within a thin gap. part 1. bubble dynamics,” *Journal of Fluid Mechanics* **704**, 211–231 (2012).



- [25] B Figueroa-Espinoza, B Mena, A Aguilar-Corona, and R Zenit, “The lifespan of clusters in confined bubbly liquids,” *International Journal of Multiphase Flow* **106**, 138–146 (2018).
- [26] Y Hallez and D Legendre, “Interaction between two spherical bubbles rising in a viscous liquid,” *Journal of Fluid Mechanics* **673**, 406–431 (2011).
- [27] F. Risso, “Physical interpretation of probability density functions of bubble-induced agitation,” *Journal of Fluid Mechanics* **809**, 240–263 (2016).